Surrogate models of heat transfer in fractured rock and their use in parameter estimation

Guofeng Song, Delphine Roubinet, Xiaoguang Wang, Gensheng Li, Xianzhi Song, Daniel Tartakovsky

Highlights

Surrogate models of heat transfer in fractured rock and their use in parameter estimation

Guofeng Song,Delphine Roubinet,Xiaoguang Wang,Gensheng Li,Xianzhi Song,Daniel M. Tartakovsky

- We present tools for estimation of statistical properties of fracture networks from cross-hole tests
- Particle-based algorithms are used to generate synthetic data for deep neural network (DNN) training
- Regionalized training strategy reduces the cost of data generation over the full parameter space
- We provide a balance analysis between DNN's generalization, accuracy and training cost

Surrogate models of heat transfer in fractured rock and their use in parameter estimation

Guofeng Song[a,b], Delphine Roubinet[c], Xiaoguang Wang[d], Gensheng Li[a], Xianzhi Song[a] and Daniel M. Tartakovsky[e,f]

[a] *State Key Laboratory of Petroleum Resources and Prospecting, China University of Petroleum, Beijing, Beijing 102249, China*
[b] *Department of Geoscience and Engineering, Delft University of Technology, Stevingweg 1, 2628CN Delft, The Netherlands*
[c] *Geosciences Montpellier (UMR 5243), CNRS, University of Montpellier, Montpellier 34090, France*
[d] *College of Energy, Chengdu University of Technology, Chengdu, 610051, China*
[e] *Department of Energy Science and Engineering, Stanford University, Stanford, CA 94305, USA*
[f] *Corresponding author*

ARTICLE INFO

Keywords:
Heat transfer
Fractured rocks
Particle tracking
Surrogate model
DFN property inversion

ABSTRACT

Fracture distribution plays a significant role in the behavior of subsurface environments, affecting such activities as geothermal production, exploitation and management of groundwater resources, and long-term storage of nuclear waste and carbon dioxide. A key challenge in these and other applications is to estimate the fracture network properties from sparse and noisy observations. We evaluate the utility of cross-borehole thermal experiments for this task, using both physics-based particle-tracking (PBPT) heat-transfer approach and deep neural network (DNN) surrogates. Synthetic data are provided by the PBPT models and used to train and test the DNN surrogates over a full range of the fracture network properties. We propose regionalized and step-by-step training techniques to reduce the computational cost of expensive PBPT forward solves over large ranges of the (to-be-estimated) parameters. Our numerical experiments suggest the feasibility of training a regionalized DNN surrogate over parameter ranges for which the PBPT solves are fast and extrapolating its predictions to parameter ranges with few additional data. We analyze the balance between computational cost and model accuracy, and provide both PBPT and DNN models for applications to others kinds of data, always considering systems in which the fractures are highly conductive structures in comparison with the matrix that is considered as impermeable to flow.

CRediT authorship contribution statement

Guofeng Song: Methodology, Software, Data Curation, Investigation, Visualization, Writing - original draft, Writing- review & editing. **Delphine Roubinet:** Conceptualization, Resources, Methodology, Supervision, Investigation, Writing- review & editing, Funding acquisition. **Xiaoguang Wang:** Conceptualization, Methodology. **Gensheng Li:** Resources, Supervision. **Xianzhi Song:** Resources, Supervision. **Daniel M. Tartakovsky:** Conceptualization, Methodology, Supervision, Writing- review & editing, Funding acquisition.

1. Introduction

Geothermal energy is a significant renewable resource that can be used for district heating and power generation (e.g., Anderson and Rezaie, 2019; Fridleifsson, 2001; Gérard et al., 2006). Most high-temperature resources are in the deep subsurface, which poses economic and technical challenges for their efficient exploitation (e.g., DiPippo, 2012; Giardini, 2009; Song et al., 2021; Wang et al., 2012). Heat extraction performance and thermal lifetime of a geothermal system are typically controlled by fracture networks (e.g., Han et al., 2020; Mahmoodpour et al., 2022; Shi et al., 2019), since they serve as main conduits for fluid flow and heat transfer. An accurate characterization of the fracture distribution provides a necessary input for the optimal design of operation schemes and hydraulic fracturing during the development of geothermal reservoirs (e.g., Pollack et al., 2021; Song et al., 2022; Xu et al., 2022). Among other applications, characterization of fractured rocks is also necessary for management and protection of groundwater resources (e.g., Carneiro, 2009; Rotter et al., 2008; Viswanathan et al., 2022).

ORCID(s): 0000-0003-3967-8735 (G. Song); 0000-0001-9019-8935 (D.M. Tartakovsky)

Information about the presence and properties of fractures are acquired with different characterization methods such as geophysical techniques (e.g., Kwiatek et al., 2014; Linde et al., 2006), hydraulic experiments (e.g., Fischer et al., 2018; Zou and Cvetkovic, 2021) and tracer tests (e.g., Cvetkovic et al., 2020; Koelbel et al., 2021; Suzuki et al., 2015; Vogt et al., 2012). Each method provides complementary information and presents its own advantages and drawbacks. For instance, the induced seismicity monitored in response to changes in injection pressure can yield an estimate of spatial changes in permeability and porosity (e.g., Kwiatek et al., 2014; Tarrahi and Jafarpour, 2012; Xu et al., 2022), while (cross-borehole) hydraulic experiments relying on flow velocity and piezometric data collected in observation wells provide information directly related to fractures intersecting the boreholes (e.g., Fischer et al., 2018; Le Borgne et al., 2006; Paillet, 1998). At larger scales, both chemical and heat tracer tests result in breakthrough curves (BTCs), whose shape and amplitude depend on the properties of the fractured domains. Chemical tracer experiments are widely used to define an equivalent representation of the systems at various scales and with various properties of the tracer (e.g., Liu et al., 2019; Kuo et al., 2018; Reimus et al., 2018). Alternatively, in thermal-tracer experiments, the water temperature in a borehole is modified by either using a heating cable or injecting hot water, and the subsequent temporal changes in temperature are monitored in the same borehole and/or a different observation borehole (e.g., Pehme et al., 2007; Klepikova et al., 2016). These thermal-tracer data have been shown to contain valuable information about the presence of fractures and the properties of either fractures or fracture-matrix configurations (e.g., de La Bernardie et al., 2018; Klepikova et al., 2016; Pehme et al., 2013). For example, synthetic data from cross-borehole thermal experiments (CBTEs) provide sufficient information about the statistical properties of fracture networks (Zhou et al., 2021). An attractive feature of thermal experiments is the ease of their implementation in the natural environment, without environmental constraints associated with solute injection in boreholes.

Regardless of the tracer type, identification of fracture network characteristics from such experiments is an inverse problem (e.g., Kang et al., 2021; Mo et al., 2020), whose solution typically requires a large number (thousands) of solves of a forward model of heat/mass transfer in multiple realizations of a discrete fracture networks (DFN). Although this problem can be simplified by considering equivalent 1D representations of discrete fracture networks (e.g., Ma et al., 2019; Xu et al., 2018; Zou et al., 2023), we focus on the inversion of the standard statistical properties of these systems. To make this computation feasible, we adopt a meshless particle-tracking (PBPT) method (Roubinet et al., 2013; Gisladottir et al., 2016) to solve flow and transport in fractured rock and use it to train a deep neural network (DNN) surrogate. The PBPT simulations are referred to as "physics-based" because they solve the differential equations encapsulating physical information such as conservation of mass, momentum, and thermal energy; this in contrast to DNNs, which map inputs on outputs without explicitly enforcing any conservation law. In a similar context, this strategy has been shown to reduce the computational burden of inverse modeling by four orders of magnitude (Zhou et al., 2021). The negligible cost of DNN surrogates makes it possible to generate large numbers of forward-model runs—corresponding to different realizations of the model parameters—that are sufficient for both accurate computation of posterior probability density functions (PDFs) and parameter estimation via such greedy algorithms as grid search methods.

An important caveat to this strategy is that DNNs yield accurate predictions of the system's behavior within the system-parameter ranges used for its training (interpolation mode), but often fail outside these ranges (extrapolation mode). The study of Zhou et al. (2021) also identifies a related challenge posed by the high cost of data generation for DNN training: it is not uncommon for the computational cost of a forward model in one parameter regime to be significantly higher than in another. Specifically, these authors found the PBPT solver to perform well for a range of two parameters (fracture density and fractal dimension) characterizing the DFN representation of Watanabe and Takahashi (1995), while experiencing convergence problems in other ranges. As a result, their DNN was trained on the PBPT output corresponding to the "good" parameter subspace, limiting its ability to estimate the DFN parameters over the whole range of the parameter variability.

To alleviate this computational bottleneck, we present a new method for the evaluation of the inverse PDFs of these parameters over the full ranges of their definition. The method employs a step-by-step regionalized technique, wherein a high-resolution DNN, first trained over a restricted range of the model parameters, is then retrained on the simulation data generated by the PBPT solver with the parameter values covering progressively larger ranges. We demonstrate our method's ability to accurately estimate statistical properties of a popular DFN representation (e.g., Bour and Davy, 1997; de Dreuzy et al., 2001; Li and Zhang, 2010; Roubinet et al., 2018; Li et al., 2009; Demirel et al., 2019). Section 2 contains a description of both the DFN representation and the PBPT method to solve fluid flow and heat transfer in fractured rock. In Section 3, we describe the architecture and training of a DNN capable of acting as a surrogate of the PBTP solver and detail our strategy for extending the DNN surrogate from one parameter subspace (in which the

Table 1
Parameter values used to generate the fracture networks.

Parameter	Value
Domain size, L	10.0 m
Minimum fracture length, $l_{\min}$	1.0 m
Minimum fracture aperture, $b_{\min}$	0.1 mm
Maximum fracture aperture, $b_{\max}$	2.5 mm
Mean of the aperture log, $\mu_{\ln b}$	−6.87
Standard deviation of the aperture log, $\sigma_{\ln b}$	0.2
Power-law exponent, a	$[1, 3]$
Percolation parameter, p	$[8, 18]$

PBPT solver is fast to execute) to another (in which it is slow). The expression of the considered inversion model and its accuracy for various definitions of the (extended) surrogate models are presented in Section 4 with the results obtained for the case of synthetic CBTE data. Discussion and conclusions are provided in Section 5.

2. Model description

2.1. Fracture network generation

We use the following strategy to generate two-dimensional fracture networks. The center of each fracture in a DFN is uniformly distributed over a square simulation domain of size L. The length, l, and aperture, b, of each fracture are randomly generated from the expressions (de Dreuzy et al., 2001; Li and Zhang, 2010; Demirel et al., 2019)

$$l = l_{\min} X^{1/(1-a)}, \qquad c = \sqrt{2}\,\sigma_c \,\mathrm{erf}^{-1}\left\{(1-X)[g(b_{\max}) - g(b_{\min})] + g(b_{\min})\right\} + \mu_c, \qquad c = \ln b \tag{1a}$$

where $l_{\min}$ is the fracture's minimum length; $b_{\min}$ and $b_{\max}$ are its minimum and maximum aperture values, respectively; natural logarithm of the aperture, $b = \exp(c)$, has the mean μ_c and the standard deviation σ_c; a is the power-law exponent; the random variable X is distributed uniformly on $U(0, 1)$; $\mathrm{erf}^{-1}(\cdot)$ is the inverse of the error function $\mathrm{erf}(\cdot)$; and

$$g(b) = \mathrm{erf}\left(\frac{\ln b - \mu_c}{\sqrt{2}\sigma_c}\right). \tag{1b}$$

Since the length, l, and aperture, b, of each fracture are mutually correlated, they are expressed in terms of the same random variable X. Fractures are added to the system until the percolation parameter

$$p = \sum_{i=1}^{N_{\mathrm{f}}} \frac{l_i^2}{L^2} \tag{2}$$

reaches a chosen value. Here, l_i is the length of the ith fracture, i.e., a realization from Eq. (1). Table 1 collates the parameter values used in our simulations and many other studies (e.g., Bour and Davy, 1997; de Dreuzy et al., 2001; Li and Zhang, 2010; Roubinet et al., 2018; Li et al., 2009; Demirel et al., 2019), the chosen domain size, $L = 10$ m, is representative of thermal dilution experiments (e.g., Klepikova et al., 2022). Two model parameters, a and p, are uncertain and given in terms of their plausible intervals of variability; values of the percolation parameter, $p \in [8, 18]$, are chosen to ensure the connectivity of the systems, since the percolation threshold is $p \sim 6$. Examples of the corresponding fracture networks are provided in Figure 1.

2.2. Physics-based model of fluid flow and heat transfer

In a CBTE, the water temperature in the left borehole is modified by either injecting warm water or using a heating cable, which induces temperature changes in the right borehole (Figure 2). These changes are monitored and reported in the form of breakthrough curves. A constant hydraulic gradient is enforced between the boreholes, and no flow condition is assumed at the top and bottom of the domain. The injected water is warmer than the ambient environment, and heat transfer between the two boreholes is the result of convection in the fractures and conduction in the matrix.

Following the standard practice, we assume the fluid flow in individual fractures to be single-phase, steady, and laminar; and the rock matrix to be impervious to the fluid. With these assumptions, average flow velocity (Darcy flux) in the ith fracture segment of the DFN, u_i, is given by the Poiseuille law (e.g., Renshaw, 1995; Adler et al., 2013),

$$u_i = -\frac{\rho g b_i^2}{12\mu} J_i, \tag{3}$$

where ρ and μ are the fluid density and dynamic viscosity, respectively; g is the gravitational acceleration constant; and J_i is the hydraulic head gradient in the ith fracture segment. By defining fracture intersections and extremities as nodes of a graph and by enforcing mass conservation at each of these nodes, one computes the values of hydraulic head at each node and flow velocity at each fracture segment (e.g., Roubinet et al., 2013, and referenes therein).

We deploy the PBPT method of Gisladottir et al. (2016) to model heat transfer by advection in fractures and conduction in the ambient matrix. While other particle-tracking techniques have been used to solve heat-transfer problems (e.g., Emmanuel and Berkowitz, 2007; Geiger and Emmanuel, 2010), our method's advantage stems from its utilization of semi-analytical expressions (Ruiz Martinez et al., 2014). That enables one to account for the effect of the matrix block size on diffusion without meshing the matrix domain, greatly reducing the computational cost in comparison with standard numerical methods. Heat transfer between the injection and observation boreholes is simulated by injecting N_{par} particles on the left side of the domain and recording their arrival times, τ_n ($n = 1, \dots, N_{\text{par}}$), on the right side. These data are then used to estimate the cumulative distribution function (CDF), $F_{\mathcal{T}}(\tau) = \mathbb{P}[\mathcal{T} \leq \tau]$, of the particle arrival time $\mathcal{T}$, which is treated as a random variable. The CDF $F_{\mathcal{T}}(\tau)$ coincides with the temporal change in the relative temperature,

$$T^*(t) = \frac{T_{\text{obs}}(t) - T_{\text{in}}}{T_{\text{inj}} - T_{\text{in}}}, \tag{4}$$

at the observation borehole. Here, T_{in} is the initial fluid temperature in the system; and T_{inj} and T_{obs} are the temperatures in the injection and observation boreholes, respectively. The relative temperature $T^* = T^*(t)$ is indeed a CDF because it is a non-negative function that varies monotonically from 0 to 1; at the beginning ($t = 0$) and the end ($t = t_{\text{end}}$) of the experiment, $T_{\text{obs}}(0) = T_{\text{in}}$ and $T_{\text{obs}}(t_{\text{end}}) = T_{\text{inj}}$, respectively. Figure 3 shows examples of these CDFs for various values of the DFN parameters $\mathbf{m} = (p, a)$. These results show that increasing the parameters p and a results in decreasing and increasing the arrival times, respectively (Figures 3a-b). As shown in Figure 1 (first column), increasing p for a given value of a results in adding fractures that create smaller matrix blocks in which the diffusion is limited, and thus the late arrival times are reduced (Figure 3a). Increasing a for a given value of p results in a different behavior, where in this case the addition of small fractures results in fracture segments with small flow velocities (Figure 1, first row), which increase the particle arrival times (Figure 3b).

3. DNN surrogates

For the CDF $F_{\mathcal{T}}(\tau) : [0, t_{\text{end}}] \to [0, 1]$ or, equivalently, $T^*(t) : [0, t_{\text{end}}] \to [0, 1]$, we define the inverse CDF (iCDF) $t = Q(T^*) : [0, 1] \to [0, t_{\text{end}}]$. This iCDF curve is represented by $N_{\text{dis}} = 50$ discretization points,

$$Q(T^*) : \{Q_1, \dots, Q_{N_{\text{dis}}}\}, \qquad Q_n = Q(T_n^*), \quad T_n^* = \frac{n}{N_{\text{dis}}}, \quad n = 1, \dots N_{\text{dis}}. \tag{5}$$

Examples of iCDFs are shown in Figures 3 for various values of the fracture network parameters $\mathbf{m}$. We consider a DNN that takes the DFN parameters $\mathbf{m} = (p, a)$ as input and returns the iCDF $Q(T^*)$ as output. In our experiments, the DNN returns a monotonic function $Q(T^*)$, even though no explicit monotonicity constraint is enforced during its training.

Table 2
Parameters related to the FCCN definition with their corresponding search region being uniformly sampled from either a discrete set of values, $U\{\cdot,\cdot,\dots,\cdot\}$, or an interval, $U[\cdot,\cdot]$, as described in Zhou et al. (2021).

FCCN parameter	Search region
Number of layers	$U\{3,4,5,6\}$
Number of neurons	$U\{2^2,2^3,...,2^9\}$
Optimizer name	$U\{\texttt{rms},\texttt{sgd},\texttt{ada},\texttt{adam}\}$
Learning rate, l_r	$\log_{10}(l_r) \sim U[-4,-2]$

3.1. Fully connected neural network

Our framework allows for different DNN architectures; we demonstrate it on a fully connected neural network (FCNN) implemented with the Python package PyTorch (Paszke et al., 2019). Let $\mathbf{d} = (d_1, \dots, d_{N_{\text{dis}}})$, where $d_n = Q_n$ with $n = 1, \dots, N_{\text{dis}}$, denote the PBPT solution in Eq. (5); and $\hat{\mathbf{d}} = \text{FCNN}(\mathbf{m}; \boldsymbol{\Theta})$ denote its estimate obtained via the FCNN. The weights of this FCNN, $\boldsymbol{\Theta}$, are obtained by minimizing the discrepancy between $\mathbf{d}$ and $\hat{\mathbf{d}}$,

$$\boldsymbol{\Theta} = \underset{\boldsymbol{\Theta}}{\text{argmin}}\, \boldsymbol{\Lambda}(\mathbf{d}, \hat{\mathbf{d}}). \tag{6}$$

The loss function $\boldsymbol{\Lambda}$ represents the discrepancy between two distributions, Q and $\hat{Q}$, or, more precisely, their discretized versions $\mathbf{d}$ and $\hat{\mathbf{d}}$. Among several alternative metrics, we select the Hellinger distance (Le Cam, 2012),

$$\boldsymbol{\Lambda}(\mathbf{d}, \hat{\mathbf{d}}) = \frac{1}{\sqrt{2}} \| \sqrt{\mathbf{d}} - \sqrt{\hat{\mathbf{d}}} \|_2 = \left[\frac{1}{2} \sum_{n=1}^{N_{\text{dis}}} \left(\sqrt{d_n} - \sqrt{\hat{d}_n} \right)^2 \right]^{1/2}. \tag{7}$$

The parameters defining the architecture of our FCNN are provided in Table 2. A precise description of this architecture is provided in (Zhou et al., 2021).

3.2. Strategy for surrogate model extension

Figure 4 shows the simulation times $\mathcal{T}_{\text{sim}}$ required to generate the fracture network and solve the fluid flow and heat transfer problem with the PBPT model for different values of the DFN parameters, $a \in [1.1, 3.0]$ and $p \in [8, 18]$. These simulation times represent the average values of $\mathcal{T}_{\text{sim}}$ over 20 realizations of the DFN for each parameter pair (p, a) (see Section 4 for details). The simulation time $\mathcal{T}_{\text{sim}}$ remains small for all values of $p \in [8, 18]$ as long as a is sufficiently small, $a \in [1.1, 1.8]$; outside of that interval, $\mathcal{T}_{\text{sim}}$ increases with p. The highest simulation times are observed for high values of a and p, which correspond to dense fracture networks characterized by the presence of small fractures. As shown in Figure 1 and explained in Section 2.2, large values of p and a result in increasing the number of small fractures with low flow velocities and producing smaller matrix blocks. The former feature results in longer exposure to relatively cooler rock and therefore greater loss of heat, which is expressed by a larger probability that particles diffuse into the matrix and transfer to another fracture, the transfer phenomenon being enhanced in small matrix blocks. Thus, the computational time is increased due to longer paths through which the particles travel by advection and in more opportunities to transfer from one fracture to the other by diffusing through matrix blocks.

We define three regions in the (p, a) parameter space (Figure 5): "small range" (SR) corresponds to small values of $\mathcal{T}_{\text{sim}}$ (mostly $\sim$ 1 s, with few values as large as 10 s) and has a rectangular shape $(p, a) \in [8, 18] \times [1.1, 1.8]$ (Figure 5a); "medium range" (MR) corresponds to intermediate values of $\mathcal{T}_{\text{sim}}$ (mostly ranging from 1 s to 10 s) and is defined by a polynomial expression $a = a(p)$ in Figure 5b; and "large range" (LR) corresponds to the values of $\mathcal{T}_{\text{sim}}$ ranging from 10 s to 100 s and is defined by a polynomial expression $a = a(p)$ in Figure 5c. The SR, MR, and LR regions occupy 36.84%, 66%, and 88.95% of the parameter space $(p, a) \in [8, 18] \times [1.1, 3.0]$, respectively (Table 3). We investigate how the simulation time and model accuracy can be optimized by working with (low-cost) regionalized models defined over a large number of data and extended to the full range of parameters with fewer data.

Table 3
Characteristics of the SR (small-range), MR (medium-range) and LR (large-range) surrogates: $a_{\max}$ is the maximum value considered for the power-law exponent parameter a; β is the proportion of the parameter ranges that is considered when varying a from 1.1 to 3 and p from 8 to 18; N_{data} is the number of PBPT solutions; $\mathcal{T}_{\text{sim}}$ is the simulation time (in hours); and ε_{red} and $\varepsilon_{\text{full}}$ are the mean training losses for the surrogates over the reduced and full ranges of parameters, respectively.

			Regionalized models				Extended models		
	$a_{\max}$	β	N_{data}	$\mathcal{T}_{\text{sim}}$	ε_{red}	ε_{ful}	N_{data}	$\mathcal{T}_{\text{sim}}$	ε_{ful}
SR model	1.8	36.84%		7.35	0.118	0.286			0.102
MR model	10 s	66%	10,000	21	0.101	0.471	3,000	93.6	0.101
LR model	100 s	88.95%		134.5	0.096	0.161			0.0997

4. Results

4.1. Surrogate model assessment

Besides the Hellinger loss in (7), we evaluate the accuracy of the FCNN model over the full ranges of parameters (p, a) in terms of the relative error

$$\mathcal{E} = \sqrt{\sum_{n=1}^{N_{\text{dis}}} (d_n - \hat{d}_n)^2} \Big/ \sqrt{\sum_{i=1}^{N_{\text{dis}}} d_i^2}, \tag{8}$$

where $\mathbf{d} = (d_1, \dots d_{N_{\text{dis}}})$ and $\hat{\mathbf{d}} = (\hat{d}_1, \dots \hat{d}_{N_{\text{dis}}})$ are the discretized inverse CDFs computed via the PBPT method and its FCNN surrogate, respectively, for a pair of the DFN parameters (p, a) not used in the FCNN training. As in Zhou et al. (2021), the efficiency of the surrogate models is evaluated by computing the conditional PDF

$$f_{\mathbf{m}|\mathbf{d}}(\tilde{\mathbf{m}}; \tilde{\mathbf{d}}) = \frac{f_{\mathbf{d}|\mathbf{m}}(\tilde{\mathbf{m}}; \tilde{\mathbf{d}})}{f_{\mathbf{d}}(\tilde{\mathbf{d}})}, \tag{9}$$

with the likelihood function

$$f_{\mathbf{d}|\mathbf{m}}(\tilde{\mathbf{m}}; \tilde{\mathbf{d}}) = \frac{1}{\sqrt{2\pi}\sigma_d} \exp\left[-\frac{1}{2\sigma_d^2} \mathbf{\Lambda}(\tilde{\mathbf{d}}, Q(\tilde{\mathbf{m}}))\right] \tag{10}$$

and the normalizing factor

$$f_{\mathbf{d}}(\tilde{\mathbf{d}}) = \int f_{\mathbf{d}|\mathbf{m}}(\tilde{\mathbf{m}}; \tilde{\mathbf{d}})\, \mathrm{d}\tilde{\mathbf{m}}. \tag{11}$$

Here, $\tilde{\mathbf{d}}$ and $\tilde{\mathbf{m}}$ are the deterministic outcomes of random variables $\mathbf{d}$ and $\mathbf{m}$, respectively; σ_d is the standard deviation (set to 0.4 hereinafter, corresponding to the measurement noise) of the PDF $f_{\mathbf{d}|\mathbf{m}}$ that is centered on the square root of the Hellinger distance $\mathbf{\Lambda}$ between the data $\tilde{\mathbf{d}}$ and the prediction of the forward model (5), $Q(\tilde{\mathbf{m}})$.

4.2. Regionalized surrogate models

The regionalized models described in Table 3 are trained on 10,000 realizations of the PBPT method for different values of parameters a and p that are randomly drawn from the SR, MR, and LR regions (Figure 5). Out of the 10,000 simulations, 8,000 are used to train the surrogate models and 2,000 to test the model accuracy. The times required to run these simulations are 7.35, 21, and 134.5 hours for the SR, MR, and LR models, respectively; the increase from the SR model to the LR models is related to the increase in the size of the domain definition that results in larger

computational times (Figure 4). In the following, these models are first applied to the range of parameters over which they have been defined, and then over the full range of parameters (i.e., $1.1 \leq a \leq 3$ and $8 \leq p \leq 18$).

Applying these models to the range of parameters over which they are defined results in the (examples of) prediction curves in Figure 6. The comparison with the BTCs computed via the reference PBPT solver shows that the FCNN surrogates accurately reproduce the training data, resulting in small training errors ϵ_{red} (Table 3) for the SR, MR, and LR surrogates.

These regionalized FCNN surrogates are deployed to compute the posterior PDF $f(\tilde{\mathbf{m}}; \tilde{\mathbf{d}})$ of parameters p and a; during NN training, these parameters are sampled over their domain of definition; Figure 7 provides three examples of these PDFs for each kind of model (SR, MR and LR), for several realizations of the DFN parameters a and p drawn randomly from the domain of definition of the surrogates. The reference values of parameters (p, a) are represented by a blue point in each plot. Figure 7 also shows the corresponding posterior PDFs obtained from 10,000 realizations of the PBPT model. The computational cost of a FCNN prediction is negligible, such that 10^7 FCNN runs—used in our FCNN estimation of the posterior PDFs in Figure 7—carry the same computational cost as the 10^4 PBPT model runs do. Hence, the use of a NN surrogate to compute a posterior PDF presents several advantages. First, it improves the estimation quality of posterior PDFs, allowing one to accurately delineate the regions of high probability (shown in deep red), which is essential for accurate inversion. Second, it enables one to extend the definition range of the PDF $f_{\mathbf{m}|\mathbf{d}}$ out of its initial domain definition with consistent values that can be used for inversion purpose. For all the examples in Figure 7, the reference point (true value) is located in the highest probability zone, as it should. The sole exception is the first example of the SR model, in which the reference point is located near the highest probability zone. In this case, although the 10,000 realizations of the reference PBPT model are located in the smallest range of the parameters considered, the resulting function is not sufficiently well defined to train the FCNN surrogate and more data might be necessary.

We first attempted to train and test the surrogate models on the data generated with 3000 model runs, for the parameter values of a and p drawn randomly from their full definition domain. The resulting DNN surrogate was computationally expensive to build and exhibited poor performance; this attempt motivated the development of our regionalized approach. In all our numerical experiments, the limiting factor is computational time rather than memory. The simulations were performed on nodes composed of 28 cores (dual Intel Xeon E5-2680 v4 2.4 Ghz Broadwell processors 2×14 cores/nodes) with 128G of allocated memory.

4.3. Extrapolation to extended domains

To test the extrapolation (aka generalization) power of the regionalized FCNN surrogates we use them to predict iCDFs for values of (p, a) that fall outside the parameter regions on which these FCNNs have been trained. Figure 8 shows representative examples of iCDFs computed for $(p, a) = (16.72, 1.75)$, $(13.03, 1.31)$, $(11.17, 2.76)$, and $(17.20, 2.84)$, which were randomly drawn from the full parameter range. The first two (p, a) pairs are from the three domains defined in Figure 5, while the third pair falls within the large range (LR) and the fourth pair does not belong to any of the three ranges. All three regionalized surrogates (SR, MR, and LR) accurately reproduce the data provided by the PBPT method for the first two pairs of (p, a), i.e., these surrogates yield accurate predictions in the interpolation mode. For the third pair of (p, a), the SR and MR surrogates slightly deviate from the reference PBPT solution, while the LR surrogate yields an accurate prediction. All three regionalized surrogates do not reproduce well the data associated with the fourth pair of reference (p, a) values. These findings confirm a well established notion that NNs do not generalize well to parameter values that are out of the training-data range.

Figure 9 exhibits the posterior PDFs, for three realizations of parameters (p, a) randomly drawn from the full range of parameters. The first (p, a) pair falls within the domains corresponding to the MR and LR models, while the second and third pairs belong to the LR region. The comparison with the reference PBPT solution demonstrates the failure of the SR surrogate to accurately reproduce the posterior PDFs in all cases. This FCNN surrogate has been trained on the reduced range of parameter a ($a < 1.8$) and does not generalize well to the situation in which the most important part of the posterior PDFs (i.e., the highest probability region) is located out of this range. Likewise, the MR surrogate yields inaccurate predictions for the remaining two reference (p, a) pairs, since these pairs fall outside the definition range of the model. The MR surrogate yields better predictions for the first pair of parameters, and the LR surrogate yields better predictions for all three pairs, since the reference (p, a) values are located within the high probability zone. However, the trend observed in the reference PBPT solution is not well captured over the whole domain. These results are confirmed by both the relatively high mean training loss ϵ_{ful} (Table 3) and the error maps in Figure 10, which reveal that the error is highest in regions of the (p, a) space that are not included in the initial definition of the surrogates.

4.4. Extended NN surrogate

Our study demonstrates that regionalized surrogates defined in the context of thermal experiments can be corrected with a relatively small number of additional PBPT simulations (about 1/3 of the initial number of simulations) defined over the full range of parameters. We supplemented the original $N_{\text{data}} = 10000$ PBPT runs with 3000 PBPT simulations carried out for the (p, a) values randomly drawn from the full parameter range. These additional simulations took 93.6 hours, as reported in Table 3. We used 2400 of the 3000 additional simulations to retrain the regionalized surrogates, and the remaining 600 simulations to test the resulting extended surrogates. The mean training losses, ε_{ful}, for the extended SR, MR, and LR surrogates are reported in Table 3. They are similar to those of the regionalized models applied to their restricted parameter ranges (ε_{red}), and significantly better than their counterparts for the regionalized models applied to the full range of parameters (ε_{ful} for regionalized models). This improvement translates into more accurate predictions of iCDFs (Figure 11). These results correspond to the same parameter pairs (p, a), for which the regionalized surrogates in Figure 8 failed to perform adequately.

This NN-training strategy also greatly improves the estimation of posterior PDFs (Figure 12) in comparison with the results presented in Figure 9. In all cases considered, the reference parameter pairs (p, a) are located in the highest probability zones and the trends observed in the reference PBPT solutions are reproduced by the FCNN surrogates. The map of errors between the reference PBPT solutions and the extended FCNN surrogates for the full range of parameters (right column in Figure 10) shows these errors to be small and uniformly distributed over the parameter space. We also observe that the extended SR, MR, and LR surrogates are equally improved by the additional training step. This performance is reminiscent of strategies for NN training on multi-fidelity data, which aim to reduce the cost of training-data generation (Song and Tartakovsky, 2021).

5. Conclusions

We introduced an efficient way to train DNN surrogates on data from simulated thermal experiments in fractured rock. Our regionalized and sequential training techniques enable one to handle wide ranges of fracture parameters, including those giving rise to computationally expensive PBPT models. The surrogates were used to estimate posterior PDFs of thermal breakthrough curves with high degree of accuracy; such PDFs are required for Bayesian data assimilation and estimation of statistical properties of fracture networks. Quantitative error maps were obtained to evaluate the reliability of prediction and inversion. Our study leads to the following major conclusions.

- DNN surrogates can be trained for parameter ranges associated with low computational cost of data generation; their subsequent extensions to wider ranges require relative few additional data.
- Such regionalized DNNs, trained on narrow parameter ranges, yield accurate predictions for parameters from those ranges, but their extrapolation to other parameter ranges results in high errors and inconsistent posteriors.
- DNN surrogates trained on about 60% of the parameter space strike an optimal balance between computational cost and inversion performance.
- Fracture percolation p and power-law exponent a determine the variability of the arrival (breakthrough) time. Generally, larger values of p and smaller values of a accelerate the thermal breakthrough.
- High computational cost of thermal models with large values of p and a precludes the ensemble physics-based computation in these ranges, $p \in [8, 18]$ and $a \in [1.1, 3]$. DNN surrogates are invaluable for this purpose.

These conclusions are drawn for the practical ranges of fracture-network parameters (p, a), while having other characteristics—minimum ($b_{\min}$) and maximum ($b_{\max}$) fracture apertures, and the mean ($\mu_{\ln b}$) and standard deviation ($\sigma_{\ln b}$) of log-normally distributed fracture aperture b—fixed at their representative values (Table 1). One could increase the dimensionality of the parameter space from 2 (used in this study) to 6, turning these parameters into the DNN input, and to draw realizations of this input from distributions other than log-normal. Our previous results (Zhou et al., 2021) show that keeping the aperture constant (and log-normally distributed) for all fractures does not impact the prediction accuracy of DNN surrogates. In field applications of our methodology, the choice of a distribution for b and its statistics should be dictated by expert knowledge and/or site-specific information.

In a follow-up study, we will use regionalized DNN surrogates to invert thermal data collected at several field experiments, starting with thermal dilution experiments at the Grimsel Test Site (Klepikova et al., 2022). We will

investigate whether the construction of new surrogates is required, and whether it can be done via transfer learning (Song and Tartakovsky, 2021) to significantly reduce the data generation and DNN training costs. Extensions of our work to chemical tracer experiments and 3D simulations are another area of future research, which would rely on physics-based models for 3D fracture networks (De Simone et al., 2023) to generate training data. Estimation of the minimal number of physics-based simulations required to generate data in the initial and extended parameter ranges has to be done to optimize the computational cost; this is especially so when dealing with expensive 3D simulations.

Acknowledgments

The authors would like to acknowledge the Project supported by France-Stanford Collaborative Center (Grant No. 165741), National Natural Science Foundation of China (Grant No. 51911530239), and the PRC-CNRS Joint Research Project Number 5181101856. This work has been realized with the support of MESO@LR-Platform at the University of Montpellier.

Code availability

Name of the code: inversion_real_DFN

Contact: guofeng_song1996@163.com or tartakovsky@stanford.edu

Hardware requirements: Thermal curves pre-processing is conducted in Pycharm Community Edition 2021.3. NN and inversion codes are operated in Google Colab.

Program language: Python

The source codes are available for downloading at https://github.com/Guofeng-Song/inversion_real_DFN.git.

References

Adler, P.M., Thovert, J.F., Mourzenko, V.V., 2013. Fractured Porous Media. EBSCO ebook academic collection, OUP Oxford.

Anderson, A., Rezaie, B., 2019. Geothermal technology: Trends and potential role in a sustainable future. Applied Energy 248, 18–34.

Bour, O., Davy, P., 1997. Connectivity of random fault networks following a power law fault length distribution. Water Resources Research 33, 1567–1583.

Carneiro, J.F., 2009. Numerical simulations on the influence of matrix diffusion to carbon sequestration in double porosity fissured aquifers. International Journal of Greenhouse Gas Control 3, 431–443. doi:10.1016/j.ijggc.2009.02.006.

Cvetkovic, V., Poteri, A., Selroos, J.O., Zou, L., 2020. Inference of retention time from tracer tests in crystalline rock. Water Resources Research 56, e2019WR025266. doi:10.1029/2019WR025266.

De Simone, S., Bour, O., Davy, P., 2023. Impact of matrix diffusion on heat transport through heterogeneous fractured aquifers. Water Resources Research 59, e2022WR033910. doi:10.1029/2022WR033910.

Demirel, S., Irving, J., Roubinet, D., 2019. Comparison of REV size and tensor characteristics for the electrical and hydraulic conductivities in fractured rock. Geophysical Journal International 216, 1953–1973.

DiPippo, R., 2012. Geothermal power plants: principles, applications, case studies and environmental impact. Butterworth-Heinemann.

de Dreuzy, J.R., Davy, P., Bour, O., 2001. Hydraulic properties of two-dimensional random fracture networks following a power law length distribution: 1. Effective connectivity. Water Resources Research 37, 2065–2078.

Emmanuel, S., Berkowitz, B., 2007. Continuous time random walks and heat transfer in porous media. Transport in Porous Media 67, 413–430. doi:10.1007/s11242-006-9033-z.

Fischer, P., Jardani, A., Lecoq, N., 2018. Hydraulic tomography of discrete networks of conduits and fractures in a karstic aquifer by using a deterministic inversion algorithm. Advances in Water Resources 112, 83–94.

Fridleifsson, I.B., 2001. Geothermal energy for the benefit of the people. Renewable and Sustainable Energy Reviews 5, 299–312.

Geiger, S., Emmanuel, S., 2010. Non-fourier thermal transport in fractured geological media. Water Resources Research 46. doi:10.1029/2009WR008671.

Gérard, A., Genter, A., Kohl, T., Lutz, P., Rose, P., Rummel, F., 2006. The deep EGS (enhanced geothermal system) project at Soultz-sous-Forêts (Alsace, France). Geothermics 35.

Giardini, D., 2009. Geothermal quake risks must be faced. Nature 462, 848–849.

Gisladottir, V.R., Roubinet, D., Tartakovsky, D.M., 2016. Particle methods for heat transfer in fractured media. Transport in Porous Media 115, 311–326.

Han, S., Cheng, Y., Gao, Q., Yan, C., Zhang, J., 2020. Numerical study on heat extraction performance of multistage fracturing enhanced geothermal system. Renewable Energy 149, 1214–1226.

Kang, X., Kokkinaki, A., Kitanidis, P.K., Shi, X., Lee, J., Mo, S., Wu, J., 2021. Hydrogeophysical characterization of nonstationary DNAPL source zones by integrating a convolutional variational autoencoder and ensemble smoother. Water Resources Research 57, e2020WR028538.

Klepikova, M., Brixel, B., Roubinet, D., 2022. Analysis of thermal dilution experiments with distributed temperature sensing for fractured rock characterization. Journal of Hydrology 610, 127874. doi:10.1016/j.jhydrol.2022.127874.

Klepikova, M.V., Le Borgne, T., Bour, O., Dentz, M., Hochreutener, R., Lavenant, N., 2016. Heat as a tracer for understanding transport processes in fractured media: Theory and field assessment from multiscale thermal push-pull tracer tests. Water Resources Research 52, 5442–5457.

Koelbel, L., Ghergut, I., Sauter, M., Kölbel, T., Wiegand, B., 2021. Integrated approach into the characterization of the fracture network of a geothermal reservoir. Applied Geochemistry 129, 104967.

Kuo, C.H., Song, S.R., Rose, P., Liu, C.M., 2018. Reactive tracer experiments in a low temperature geothermal field, Yilan, Taiwan. Geothermics 74, 298–304.

Kwiatek, G., Bulut, F., Bohnhoff, M., Dresen, G., 2014. High-resolution analysis of seismicity induced at Berlín geothermal field, El Salvador. Geothermics 52, 98–111.

de La Bernardie, J., Bour, O., Le Borgne, T., Guihéneuf, N., Chatton, E., Labasque, T., Le Lay, H., Gerard, M.F., 2018. Thermal attenuation and lag time in fractured rock: Theory and field measurements from joint heat and solute tracer tests. Water Resources Research 54, 10–053.

Le Borgne, T., Paillet, F., Bour, O., Caudal, J., 2006. Cross-borehole flowmeter tests for transient heads in heterogeneous aquifers. Ground Water 44, 444–452. doi:10.1111/j.1745-6584.2005.00150.x.

Le Cam, L., 2012. Asymptotic methods in statistical decision theory. Springer Science & Business Media.

Li, J., Zhang, L., 2010. Geometric parameters and rev of a crack network in soil. Computers and Geotechnics 37, 466–475.

Li, J., Zhang, L., Wang, Y., Fredlund, D., 2009. Permeability tensor and representative elementary volume of saturated cracked soil. Canadian Geotechnical Journal 46, 928–942.

Linde, N., Binley, A., Tryggvason, A., Pedersen, L.B., Revil, A., 2006. Improved hydrogeophysical characterization using joint inversion of cross-hole electrical resistance and ground-penetrating radar traveltime data. Water Resources Research 42.

Liu, Y., Liu, G., Zhao, Z., Zhang, H., 2019. Theoretical model of geothermal tail water reinjection based on an equivalent flow channel model: A case study in Xianxian, North China plain. Energy Exploration & Exploitation 37, 849–864.

Ma, G., Li, T., Wang, Y., Chen, Y., 2019. The equivalent discrete fracture networks based on the correlation index in highly fractured rock masses. Engineering Geology 260, 105228. doi:10.1016/j.enggeo.2019.105228.

Mahmoodpour, S., Singh, M., Turan, A., Bär, K., Sass, I., 2022. Simulations and global sensitivity analysis of the thermo-hydraulic-mechanical processes in a fractured geothermal reservoir. Energy 247, 123511.

Mo, S., Zabaras, N., Shi, X., Wu, J., 2020. Integration of adversarial autoencoders with residual dense convolutional networks for estimation of non-gaussian hydraulic conductivities. Water Resources Research 56, e2019WR026082.

Paillet, F.L., 1998. Flow modeling and permeability estimation using borehole flow logs in heterogeneous fractured formations. Water Resources Research 34, 997–1010. doi:10.1029/98WR00268.

Paszke, A., Gross, S., Massa, F., Lerer, A., Bradbury, J., Chanan, G., Killeen, T., Lin, Z., Gimelshein, N., Antiga, L., et al., 2019. Pytorch: An imperative style, high-performance deep learning library. Advances in neural information processing systems 32.

Pehme, P., Parker, B., Cherry, J., Molson, J., Greenhouse, J., 2013. Enhanced detection of hydraulically active fractures by temperature profiling in lined heated bedrock boreholes. Journal of Hydrology 484, 1–15.

Pehme, P.E., Greenhouse, J.P., Parker, B.L., 2007. The active line source temperature logging technique and its application in fractured rock hydrogeology. Journal of Environmental and Engineering Geophysics 12, 307–322.

Pollack, A., Cladouhos, T.T., Swyer, M.W., Siler, D., Mukerji, T., Horne, R.N., 2021. Stochastic inversion of gravity, magnetic, tracer, lithology, and fault data for geologically realistic structural models: Patua geothermal field case study. Geothermics 95, 102129.

Reimus, P., Dean, C., Newell, D., 2018. Evaluation of a cation-exchanging tracer to interrogate fracture surface area in enhanced geothermal systems. Geothermics 71, 12–23.

Renshaw, C., 1995. On the relationship between mechanical and hydraulic apertures in rough-walled fractures. Journal of Geophysical Research-Solid Earth 100, 24629–24636. doi:10.1029/95JB02159.

Rotter, B.E., Barry, D.A., Gerhard, J.I., Small, J.S., 2008. Modeling U(VI) biomineralization in single- and dual- porosity porous media. Water Resources Research 44, W08437. doi:10.1029/2007WR006301.

Roubinet, D., De Dreuzy, J.R., Tartakovsky, D.M., 2013. Particle-tracking simulations of anomalous transport in hierarchically fractured rocks. Computers & Geosciences 50, 52–58.

Roubinet, D., Irving, J., Pezard, P.A., 2018. Relating topological and electrical properties of fractured porous media: Insights into the characterization of rock fracturing. Minerals 8, 14.

Ruiz Martinez, A., Roubinet, D., Tartakovsky, D.M., 2014. Analytical models of heat conduction in fractured rocks. J. Geophys. Res. Solid Earth 119, 83–98. doi:10.1002/2012JB010016.

Shi, Y., Song, X., Wang, G., Li, J., Geng, L., Li, X., 2019. Numerical study on heat extraction performance of a multilateral-well enhanced geothermal system considering complex hydraulic and natural fractures. Renewable Energy 141, 950–963.

Song, D.H., Tartakovsky, D.M., 2021. Transfer learning on multi-fidelity data. J. Mach. Learn. Model. Comput. 3, 31–47. doi:10.1615/JMachLearnModelComput.2021038925.

Song, G., Roubinet, D., Zhou, Z., Wang, X., Tartakovsky, D.M., Song, X., 2022. Estimation of statistical properties of fracture networks from thermal-tracer experiments, in: 47th Workshop on Geothermal Reservoir Engineering.

Song, G., Song, X., Li, G., Shi, Y., Wang, G., Ji, J., Xu, F., Song, Z., 2021. An integrated multi-objective optimization method to improve the performance of multilateral-well geothermal system. Renewable Energy 172, 1233–1249.

Suzuki, A., Niibori, Y., Fomin, S.A., Chugunov, V.A., Hashida, T., 2015. Fractional derivative-based tracer analysis method for the characterization of mass transport in fractured geothermal reservoirs. Geothermics 53, 125–132.

Tarrahi, M., Jafarpour, B., 2012. Inference of permeability distribution from injection-induced discrete microseismic events with kernel density estimation and ensemble Kalman filter. Water Resources Research 48.

Viswanathan, H.S., Ajo-Franklin, J., Birkholzer, J., Carey, J.W., Guglielmi, Y., Hyman, J.D., Karra, S., Pyrak-Nolte, L., Rajaram, H., Srinivasan, G., Tartakovsky, D.M., 2022. From fluid flow to coupled processes in fractured rock: recent advances and new frontiers. Rev. Geophys. 60, e2021RG000744. doi:10.1029/2021WR030608.

Vogt, C., Kosack, C., Marquart, G., 2012. Stochastic inversion of the tracer experiment of the enhanced geothermal system demonstration reservoir in Soultz-sous-Forêts—revealing pathways and estimating permeability distribution. Geothermics 42, 1–12.

Wang, J., Hu, S., Pang, Z., He, L., Zhao, P., Zhu, C., Rao, S., Tang, X., Kong, Y., Luo, L., et al., 2012. Estimate of geothermal resources potential for hot dry rock in the continental area of China. Sci. Technol. Rev 30, 32.

Watanabe, K., Takahashi, H., 1995. Fractal geometry characterization of geothermal reservoir fracture networks. Journal of Geophysical Research: Solid Earth 100, 521–528.

Xu, C., Fidelibus, C., Dowd, P., Wang, Z., Tian, Z., 2018. An iterative procedure for the simulation of the steady-state fluid flow in rock fracture networks. Engineering Geology 242, 160–168. doi:10.1016/j.enggeo.2018.06.005.

Xu, T., Liang, X., Xia, Y., Jiang, Z., Gherardi, F., 2022. Performance evaluation of the habanero enhanced geothermal system, australia: Optimization based on tracer and induced micro-seismicity data. Renewable Energy 181, 1197–1208.

Zhou, Z., Roubinet, D., Tartakovsky, D.M., 2021. Thermal experiments for fractured rock characterization: theoretical analysis and inverse modeling. Water Resources Research 57, e2021WR030608.

Zou, L., Cvetkovic, V., 2021. Evaluation of flow-log data from crystalline rocks with steady-state pumping and ambient flow. Geophysical Research Letters 48, e2021GL092741. doi:10.1029/2021GL092741.

Zou, L., Selroos, J.O., Poteri, A., Cvetkovic, V., 2023. Parameterization of a channel network model for groundwater flow in crystalline rock using geological and hydraulic test data. Engineering Geology 317, 107060. doi:10.1016/j.enggeo.2023.107060.

List of Figures

1 Examples of fracture networks for different values of parameters p and a. The color of the fractures is related to their aperture with increasing aperture from black to red. 13
2 Schematic representation of a cross-borehole thermal experiment (CBTE) in fractured rocks considering flow and heat transfer processes. 14
3 Examples of thermal (a and b) cumulative distribution functions (CDFs) and (c and d) inverse cumulative distribution functions (iCDFs) for different values of (a and c) the percolation parameter p and (b and d) power-law exponent a. These results are obtained with the PBPT method using 1000 particles. 15
4 Computational time T_c determined from the linear interpolation of the times averaged over 20 fracture network realizations and for 373 values of parameters a and p. The color bar represents the log value of the computational time. The two black lines represent the polynomial interpolations whose expressions are provided in Figure 5, the simulations being smaller than 10 and 100 seconds for the parameters located below these lines. 16
5 Definition of the (a) small, (b) medium, and (c) large ranges over which 10,000 random pairs of parameters (p, a) are drawn. The polynomial expressions that define the medium and large ranges come from the simulation times $\mathcal{T}_{\text{sim}}$ reported in Figure 4. 17
6 Examples of iCDFs computed with the reference PBPT solver (denoted as truth) and the SR (top), MR (middle), and LR (bottom) regionalized surrogate models (denoted as prediction) for several realizations of parameters a and p drawn from the definition domains of the respective models. 18
7 Examples of posterior PDFs computed with the PBPT method (first, third, and fifth rows) and the regionalized (SR, MR, and LR) FCNN surrogates (second, fourth, and sixth rows), for realizations of DFN parameters (p, a) drawn from these ranges (represented by a blue point on each figure). 19
8 Examples of iCDFs computed with the reference PBPT solution (denoted as truth) and the SR (top), MR (middle), and LR (bottom) regionalized surrogates (denoted as prediction) for realizations of (p, a) drawn from the full range of parameters. 20
9 Examples of posterior PDFs computed with the PBPT reference model (first row) and the SR, MR, and LR surrogate DNN models (second, third, and fourth rows) for reference random values of parameters a and p drawn in the full range of parameters (represented as a blue point on each figure). 21
10 Maps of the relative error ϵ defined in (8) with the regionalized (left column) and extended (right column) surrogate models applied to the full range of parameters. 22
11 Examples of iCDFs computed with the reference PBPT model (denoted as truth) and the extended surrogate SR (top), MR (middle), and LR (bottom) models (denoted as prediction) for random values of parameters a and p that are drawn in the full range of parameters. 23
12 Examples of posterior PDFs computed with the PBPT reference model (first row) and the extended SR, MR, and LR surrogates (second, third, and fourth rows) for the reference realizations of DFN parameters a and p (represented as a blue point on each figure) drawn from their full range of variability. 24

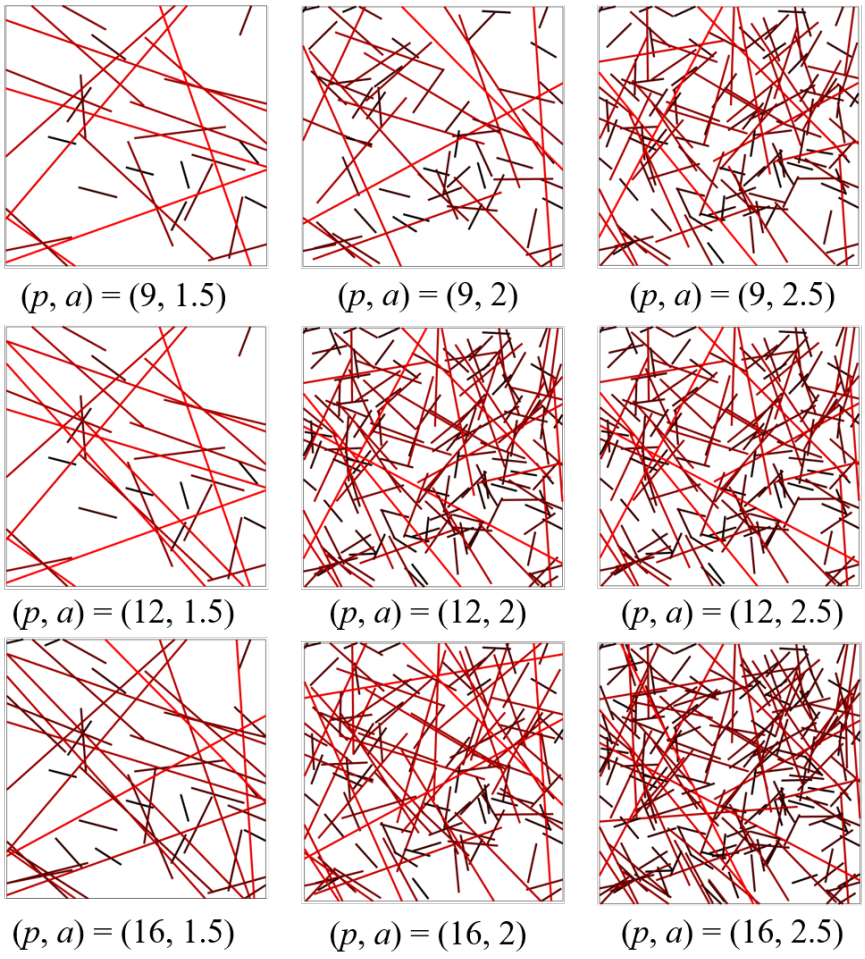

Figure 1: Examples of fracture networks for different values of parameters p and a. The color of the fractures is related to their aperture with increasing aperture from black to red.

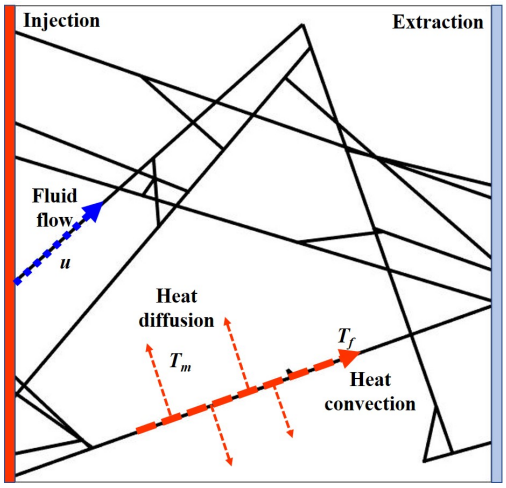

Figure 2: Schematic representation of a cross-borehole thermal experiment (CBTE) in fractured rocks considering flow and heat transfer processes.

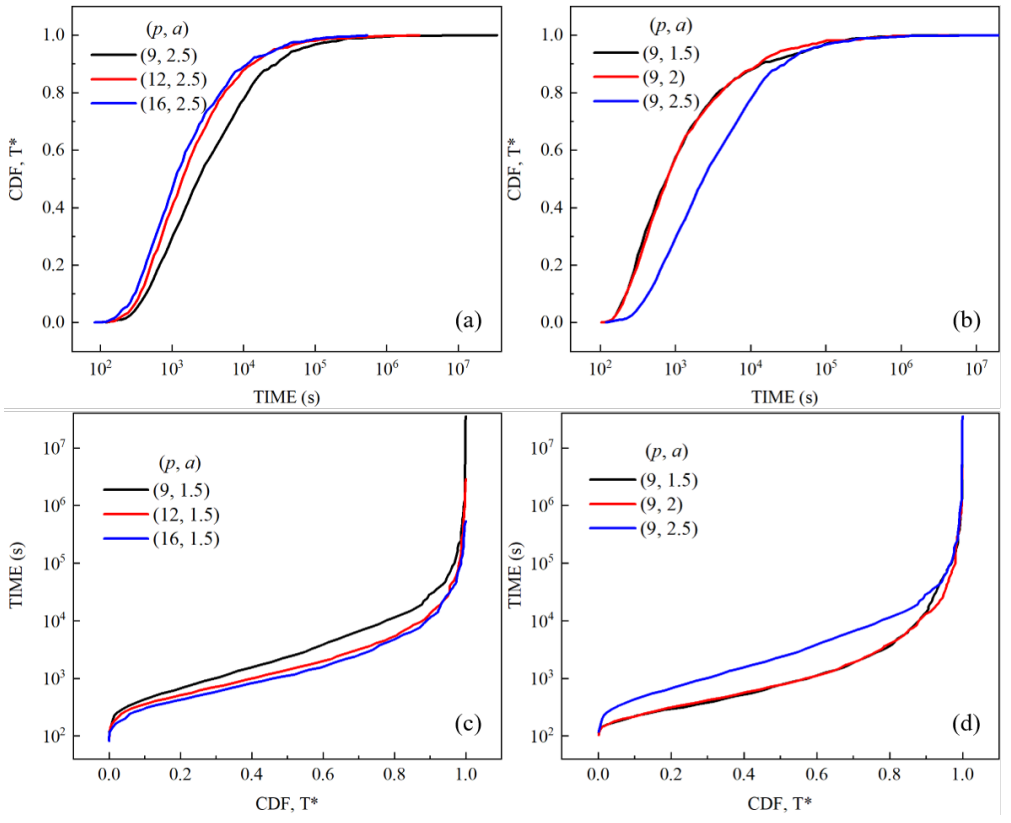

Figure 3: Examples of thermal (a and b) cumulative distribution functions (CDFs) and (c and d) inverse cumulative distribution functions (iCDFs) for different values of (a and c) the percolation parameter p and (b and d) power-law exponent a. These results are obtained with the PBPT method using 1000 particles.

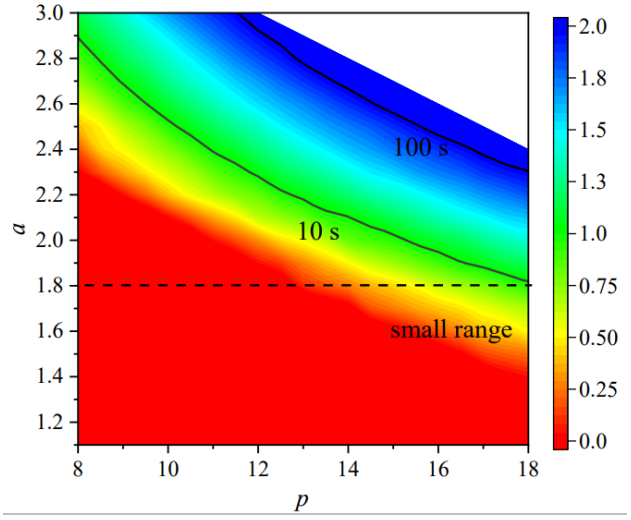

Figure 4: Computational time T_c determined from the linear interpolation of the times averaged over 20 fracture network realizations and for 373 values of parameters a and p. The color bar represents the log value of the computational time. The two black lines represent the polynomial interpolations whose expressions are provided in Figure 5, the simulations being smaller than 10 and 100 seconds for the parameters located below these lines.

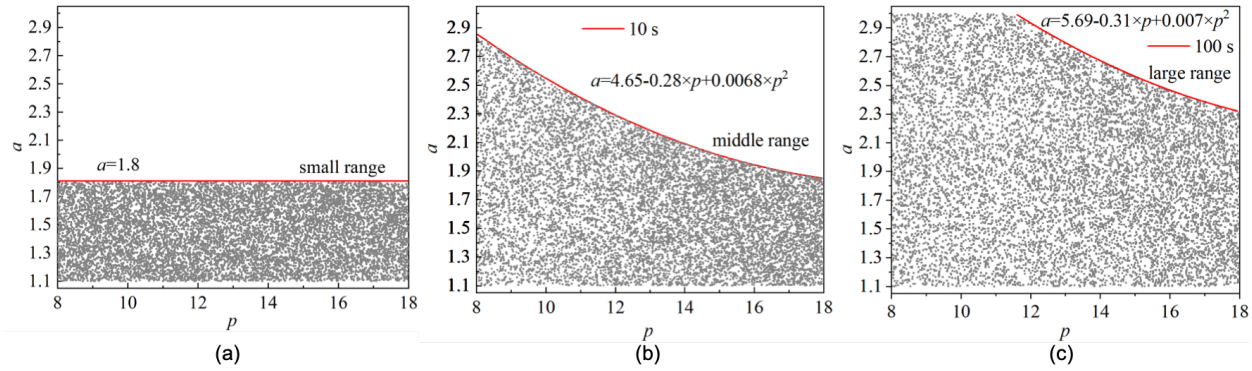

Figure 5: Definition of the (a) small, (b) medium, and (c) large ranges over which 10,000 random pairs of parameters (p, a) are drawn. The polynomial expressions that define the medium and large ranges come from the simulation times $\mathcal{T}_{\mathsf{sim}}$ reported in Figure 4.

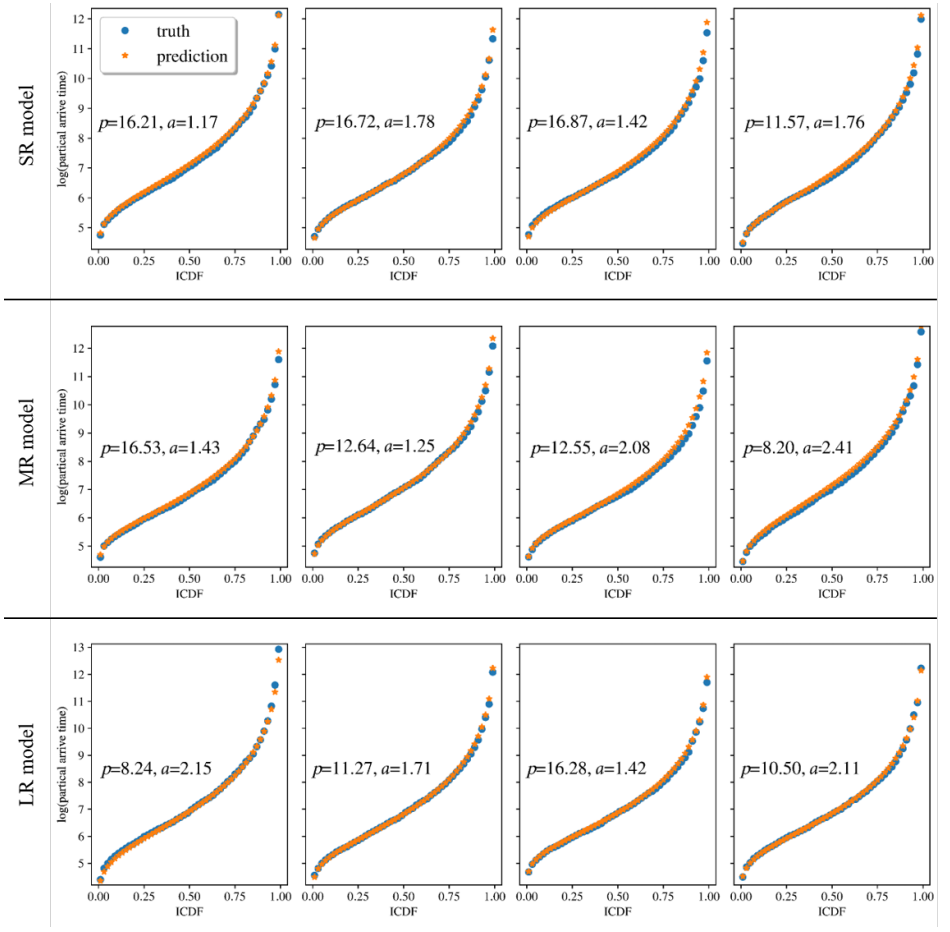

Figure 6: Examples of iCDFs computed with the reference PBPT solver (denoted as truth) and the SR (top), MR (middle), and LR (bottom) regionalized surrogate models (denoted as prediction) for several realizations of parameters a and p drawn from the definition domains of the respective models.

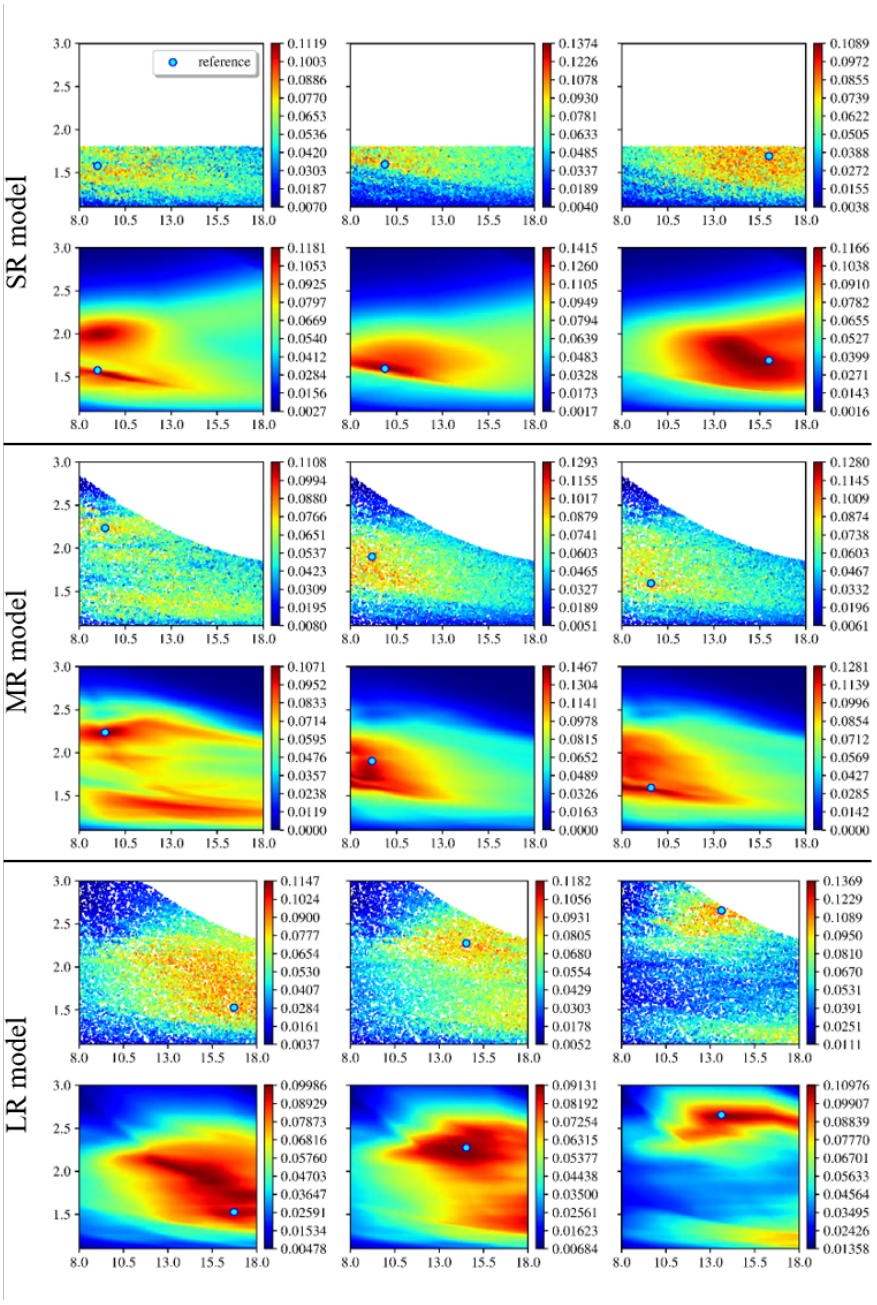

Figure 7: Examples of posterior PDFs computed with the PBPT method (first, third, and fifth rows) and the regionalized (SR, MR, and LR) FCNN surrogates (second, fourth, and sixth rows), for realizations of DFN parameters (p, a) drawn from these ranges (represented by a blue point on each figure).

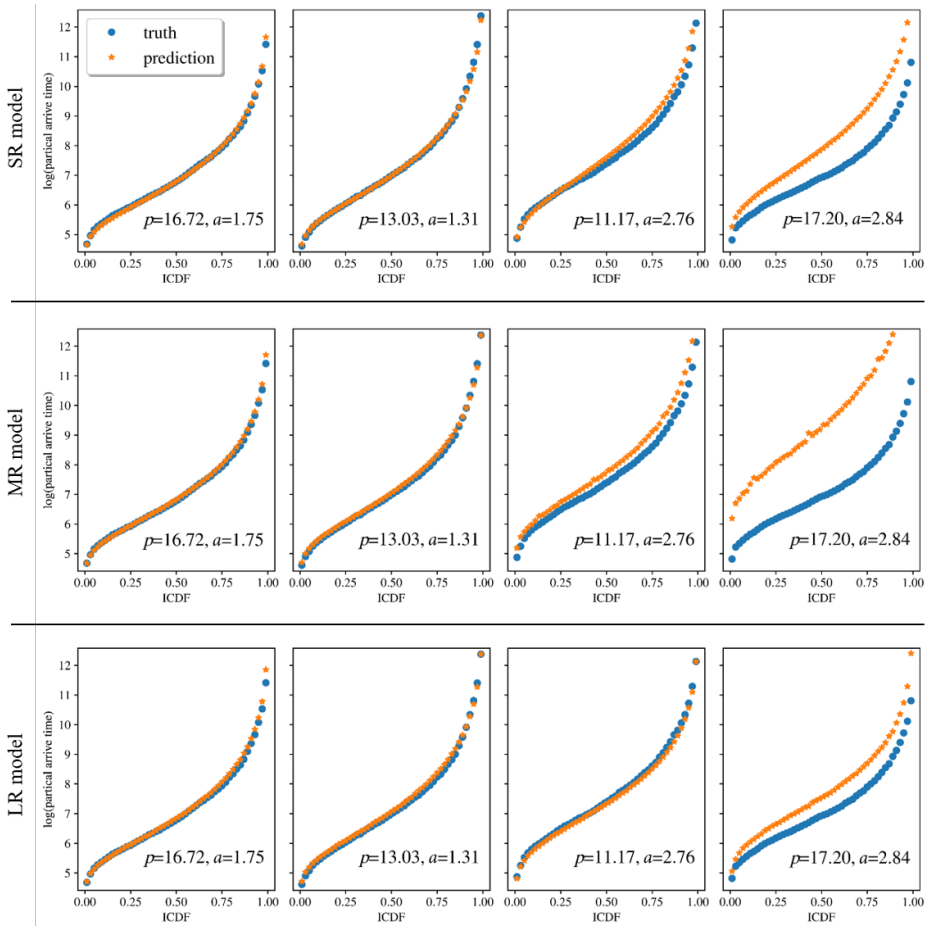

Figure 8: Examples of iCDFs computed with the reference PBPT solution (denoted as truth) and the SR (top), MR (middle), and LR (bottom) regionalized surrogates (denoted as prediction) for realizations of (p, a) drawn from the full range of parameters.

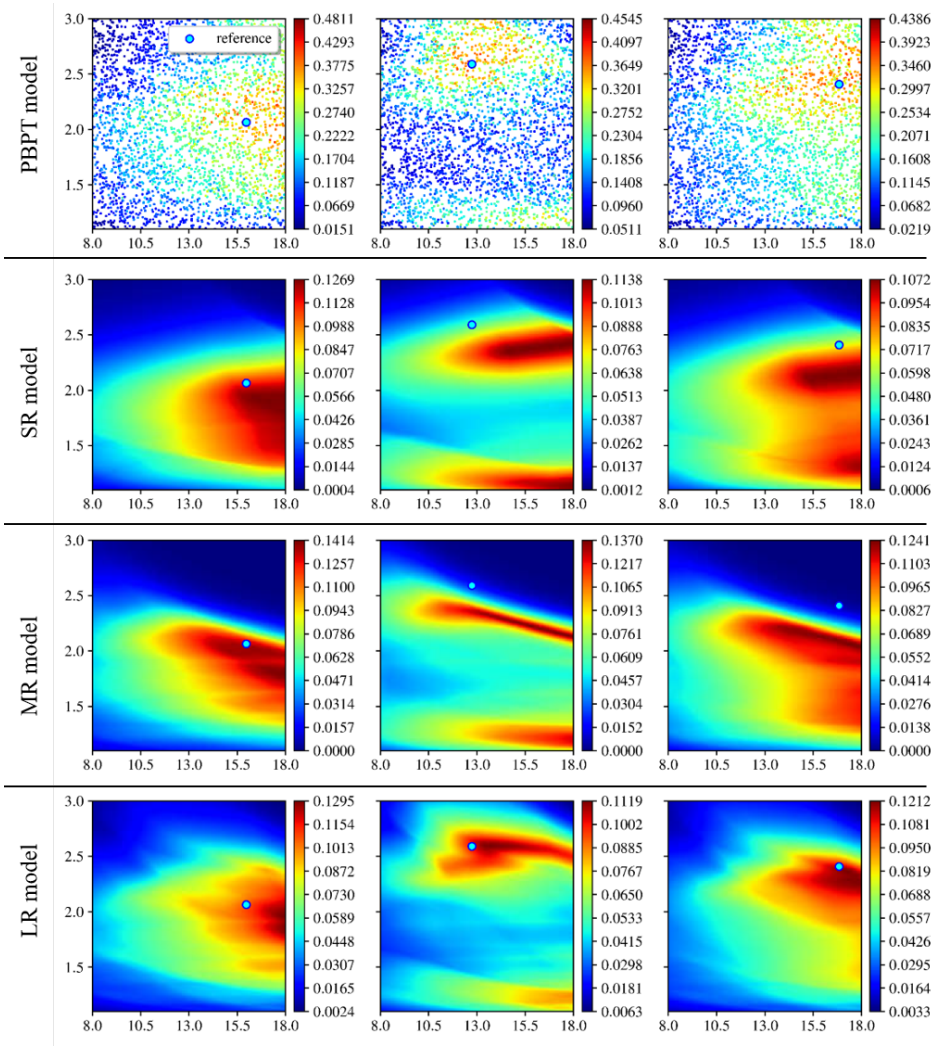

Figure 9: Examples of posterior PDFs computed with the PBPT reference model (first row) and the SR, MR, and LR surrogate DNN models (second, third, and fourth rows) for reference random values of parameters a and p drawn in the full range of parameters (represented as a blue point on each figure).

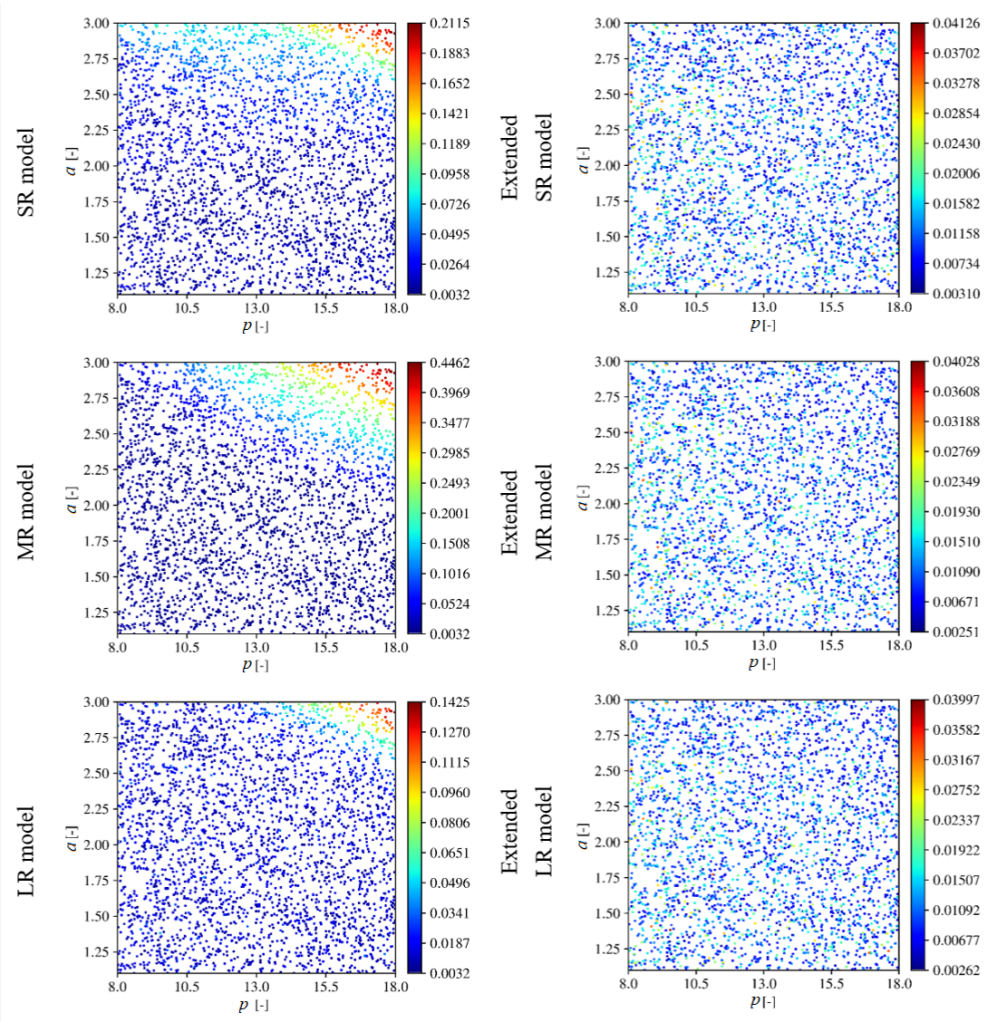

Figure 10: Maps of the relative error ϵ defined in (8) with the regionalized (left column) and extended (right column) surrogate models applied to the full range of parameters.

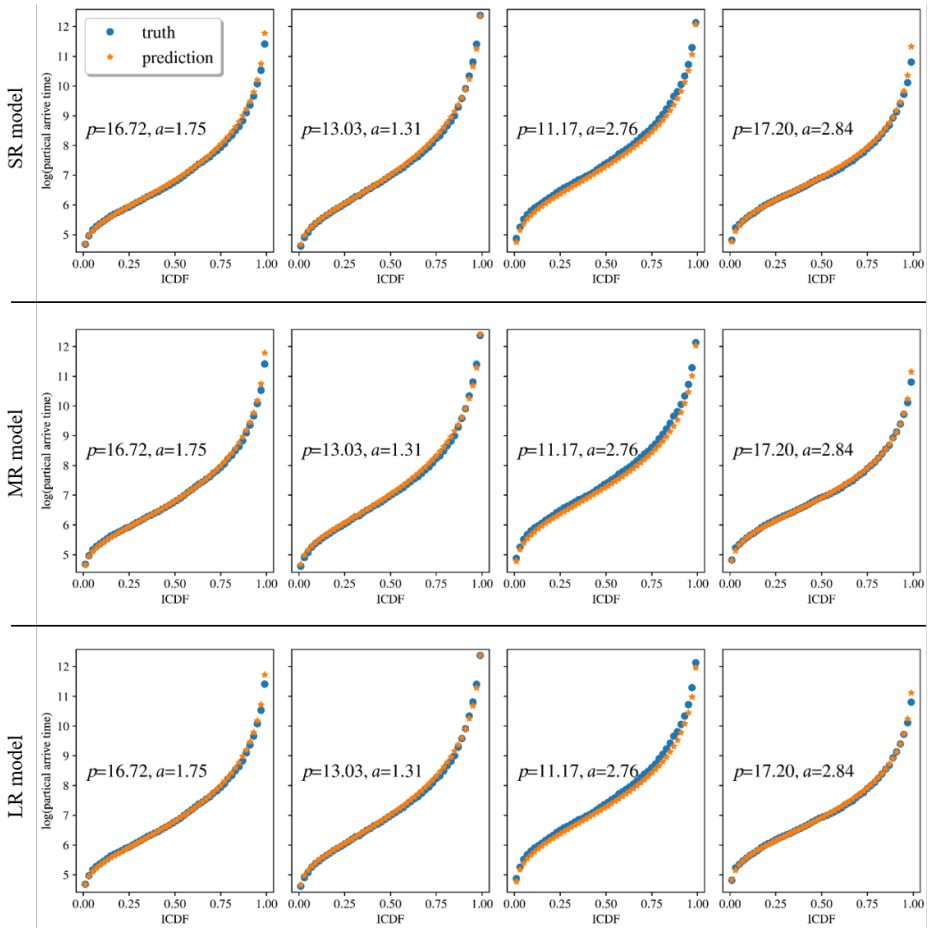

Figure 11: Examples of iCDFs computed with the reference PBPT model (denoted as truth) and the extended surrogate SR (top), MR (middle), and LR (bottom) models (denoted as prediction) for random values of parameters a and p that are drawn in the full range of parameters.

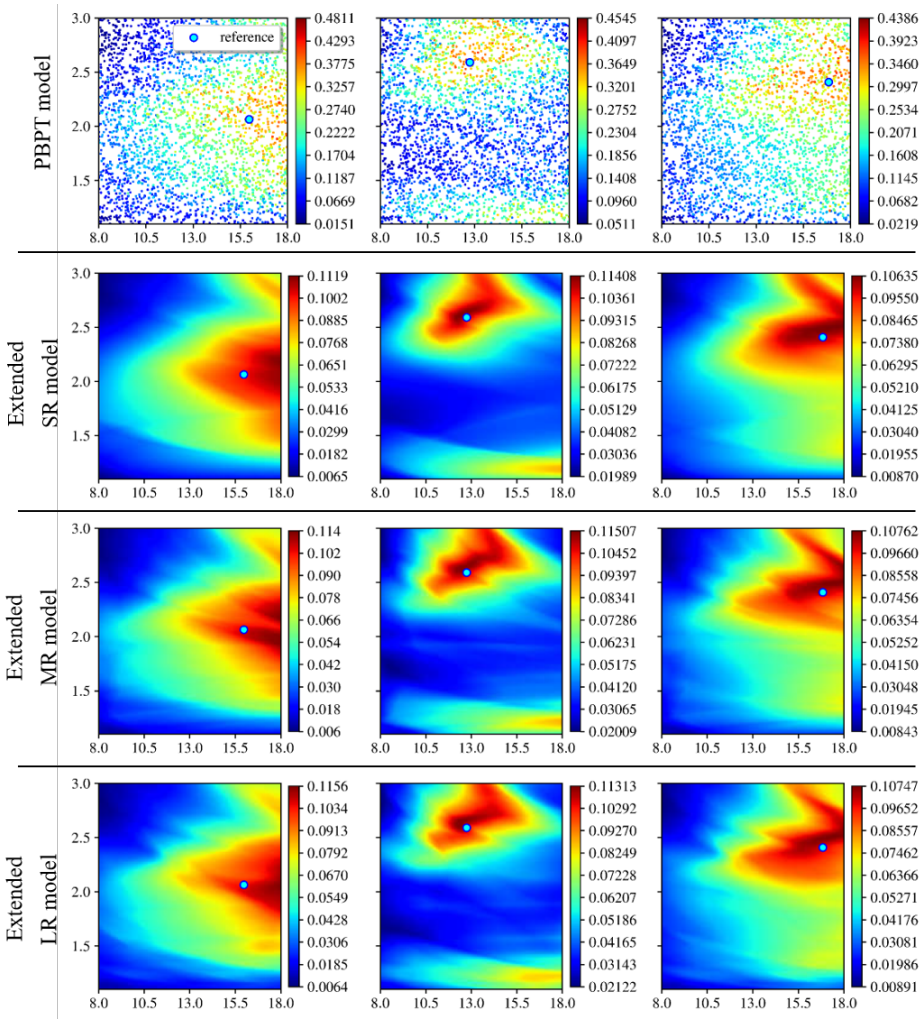

Figure 12: Examples of posterior PDFs computed with the PBPT reference model (first row) and the extended SR, MR, and LR surrogates (second, third, and fourth rows) for the reference realizations of DFN parameters a and p (represented as a blue point on each figure) drawn from their full range of variability.